nature structural & molecular biology

ARTICLES

https://doi.org/10.1038/s41594-018-0047-3

Gating interaction maps reveal a noncanonical electromechanical coupling mode in the Shaker K+ channel

Ana I. Fernández-Mariño[1,4,6], Tyler J. Harpole[2,6], Kevin Oelstrom[1,5], Lucie Delemotte[2] and Baron Chanda[1,3*]

Membrane potential regulates the activity of voltage-dependent ion channels via specialized voltage-sensing modules, but the mechanisms involved in coupling voltage-sensor movement to pore opening remain unclear owing to a lack of resting state structures and robust methods to identify allosteric pathways. Here, using a newly developed interaction-energy analysis, we probe the interfaces of the voltage-sensing and pore modules in the *Drosophila* Shaker K+ channel. Our measurements reveal unexpectedly strong equilibrium gating interactions between contacts at the S4 and S5 helices in addition to those between S6 and the S4–S5 linker. Network analysis of MD trajectories shows that the voltage-sensor and pore motions are linked by two distinct pathways: a canonical pathway through the S4–S5 linker and a hitherto unknown pathway akin to rack-and-pinion coupling involving the S4 and S5 helices. Our findings highlight the central role of the S5 helix in electromechanical transduction in the voltage-gated ion channel (VGIC) superfamily.

Electrical signaling underlies a variety of fundamental biological processes that include nerve impulses, rhythmic contraction of the heart and hormonal secretion. Members of the VGIC superfamily are primarily responsible for electrical excitability in higher organisms. They share a common structural feature wherein four discrete voltage-sensing modules surround a central pore module[1]. Each voltage-sensing module is made up of four transmembrane segments, whereas the central pore module has a total of eight transmembrane segments contributed by four subunits. Changes in membrane voltage drive the movement of the charge-carrying transmembrane segments in the voltage-sensing domain, which is coupled to the pore gate in the central pore module. Over the past decade, it has become increasingly evident that the differences in coupling between the voltage-sensor domain and the pore are crucial determinants of channel behavior[2,3].

In a definitive study, Lu and colleagues[4,5] were the first to show that the two-transmembrane-segment KcsA channel exhibits voltage-dependent activity when fused to the voltage-sensing domain of the Shaker K+ channel as long as the contacts between the S4–S5 linker and the lower S6 helix is conserved. High-resolution structures of the voltage-gated ion channels suggest a plausible model of electromechanical coupling[1,6–8]. Accordingly, the movement of the S4 transmembrane segment pushes or pulls the attached S4–S5 linker, which is in juxtaposition with a portion of the S6 helix that forms the pore gate ($S6_{CT}$). The notion that the S4–S5 linker is central to electromechanical coupling in the VGIC superfamily is supported by sophisticated structure–function studies in potassium and sodium channels that show that mutations in this intracellular gating interface alter channel gating and make voltage-dependent opening less efficient[5,9,10].

Recent studies, however, have raised new questions about the role of the S4–S5 linker and the mechanism of electromechanical coupling[11,12]. Using a split channel strategy, Lörinczi et al.[13] found that the EAG channels are still gated by voltage despite deletion of the S4–S5 linker. High-resolution cryo-EM structures of wild-type EAG channels[14] show that these channels have a non-domain-swapped architecture and that the S4–S5 linker is a short loop rather than a distinct helix as in K_v1.2–2.1 chimeras. This finding raises the possibility that the S4–S5 helix is only involved in coupling in channels with domain-swapped architecture, such as the Shaker K+ channel, whereas in non-domain-swapped configuration, there exists a noncanonical pathway that bypasses the S4–S5 linker region.

What are the alternate mechanisms for coupling between the voltage sensor and the pore? Even though the voltage sensor is a discrete and somewhat portable module, in every structure of a voltage-gated ion channel, there are residues in the voltage-sensing domain that form intimate steric contacts with residues in the S5 transmembrane helix[1,13,15–20]. While there are no structures of the same protein in both resting and activated state, comparisons of the putative resting state models and multiple structures in various conformations suggest that this interface changes with channel gating[21,22]. Previous studies have also shown that noncharged residues in this transmembrane interface account for dramatic differences in the gating behavior between different potassium channel families[23–25] mainly due to alterations in coupling. We wondered whether there is an alternate pathway for transducing voltage-sensor movement to the pore gates even in channels that have the prototypical domain-swapped architecture.

Here, we broadly probe the transmembrane and intracellular interfaces between the voltage-sensing and pore modules by

[1]Department of Neuroscience, SMPH, University of Wisconsin, Madison, WI, USA. [2]Science for Life Laboratory, Department of Applied Physics, KTH Royal Institute of Technology, Solna, Sweden. [3]Department of Biomolecular Chemistry, SMPH, University of Wisconsin, Madison, WI, USA. [4]Present address: Molecular Physiology and Biophysics Section, Porter Neuroscience Research Center, National Institute of Neurological Disorders and Stroke, National Institutes of Health, Bethesda, MD, USA. [5]Present address: Cellular Dynamics International Inc., Madison, WI, USA. [6]These authors contributed equally: Ana I. Fernández-Mariño and Tyler Harpole. *e-mail: chanda@wisc.edu

measuring how the transinteraction energies at specific contact sites change during channel activation. To this end, we combined generalized interaction-energy analysis (GIA), which is currently the most rigorous approach to experimentally measure site-specific interactions, with network analysis of molecular simulations to identify the allosteric signaling pathways. We find that in addition to contacts at the intracellular interface, the residue contacts at the transmembrane interface between the voltage-sensor domain and the pore contribute substantially to channel gating. Network analysis of molecular dynamics trajectories support our experimental findings and show that the S4 movement triggers a conformational change in the pore gate via canonical and noncanonical pathways involving contacts on the S5 helix. These experimental and computational studies provide a remarkably congruent view of signal propagation between voltage sensor and pore in a prototypical domain-swapped VGIC.

Results

Examining different interfaces with GIA. Examination of the interface between the voltage-sensing and pore modules in the $K_v1.2$–2.1 chimera structure shows that there are a number of contact points involving residues at this interface, suggesting that voltage-sensor movement relative to the pore probably alters the interactions at this interface[1,7,15,17]. Unless the net interaction energy at this interface between resting and activated states is completely balanced, the changes in these transinteractions contribute to the strength of coupling between the voltage sensor and the pore. There is no available structure of the $K_v1.2$–2.1 chimera in the resting state, but distance matrices obtained from long-time-scale MD simulations of the $K_v1.2$–2.1 channel shows that deactivation causes the S4 helices to move downward and undergo a helical screw motion (Supplementary Fig. 1 and Supplementary Dataset 1). To determine how these interactions change upon channel gating, we focused on the contact sites in the intracellular gating interface (S4–S5 linker with S4 or S6 helices) and the transmembrane gating interface formed by the S4 and S5 helices (Fig. 1).

To measure the strength of the interactions at the contact sites, we used the recently introduced GIA method[26,27]. This method measures the median voltage activity of gating charge–voltage (Q–V) curves to calculate the net activation energy of channel gating[28–30] (Methods). In contrast to conductance measurements (G–V curves), which provide the free-energy difference between the open and poorly defined intermediate states of the channel, Q–V curves allow us to calculate the free-energy difference between the two end states, namely, the initial resting state and the final activated state. Free-energy calculations based on G–V curves are highly susceptible to type I errors because mutations may alter the intermediate states without affecting the net free energy of activation[26]. Only in a two-state model do the free energies calculated from G–V curves correspond to the net free energy of activation. The GIA approach based on Q–V measurements is robust and allows us to calculate the free energy of activation without consideration of the complexity of the underlying model. In order to obtain the net free energy of activation, this median voltage value from the Q–V curve is multiplied by the total gating charge per channel. In this report, we estimated both the median voltage and the total gating charge per channel at the same time by combining fluorescence intensity measurements with gating current measurements.

Coupling clusters at intracellular gating interface. Previous studies have suggested that the mutation of residues in the S4–S5 linker modify channel gating and possibly alter electromechanical coupling strength[31–34]. On the basis of the structure, we first tested the interaction between R387 in the S4–S5 linker and F484 from the lower S6 segment. Gating current measurements revealed that the Q–V curves of F484A and the F484A R387A double mutant are

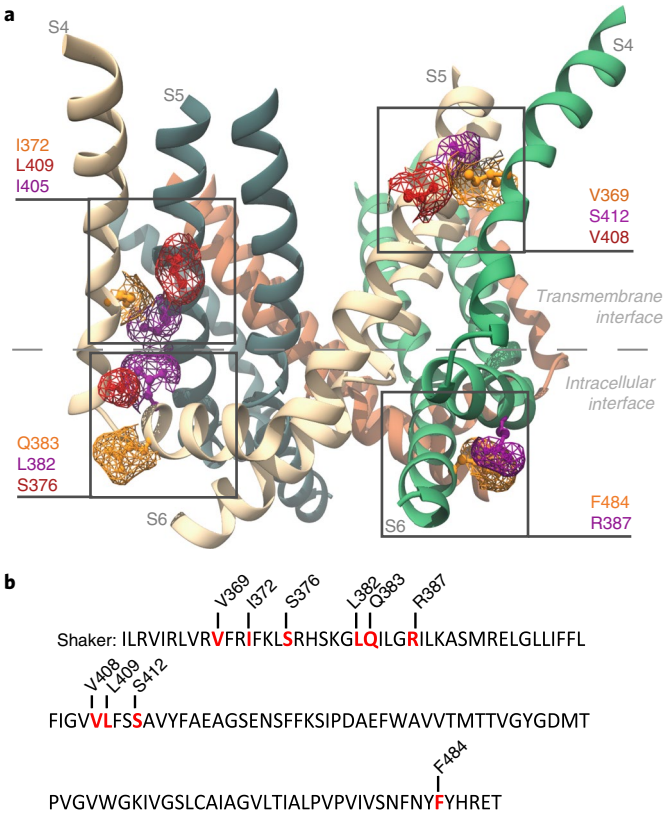

Fig. 1 | Interfacial regions and residues tested for electromechanical coupling. a, Side view of the $K_v1.2$–2.1 chimera structure (PDB 2R9R). Only S4, S4–S5 linker, S5 and S6 helices are shown for clarity. Highlighted in purple, orange and red are the residues in the transmembrane gating interface of S4 and S5 of neighboring subunits (V369 with V408 and S412; I372 with I405 and L409) and those at the intracellular gating interface (S4–S5 linker (R387) with S6 (F484) and the S4 (S376) with S4–S5 linker (L382 and Q383) of the same subunit). The residue numbering corresponds to positions in the Shaker K^+ channel (alignment in Supplementary Fig. 6). **b**, Shaker sequence from residue I360 to T489. Residues that were mutated to alanine are highlighted in red.

slightly left-shifted, whereas that of R387A shifted right compared to that of the wild type (WT) (Fig. 2 and Supplementary Dataset 2; Supplementary Table 1 and Supplementary Datasets 3 and 4). All gating current measurements were obtained in the nonconducting W434F background. Although the rightward shift for R387A was large, a corresponding rightward shift was not observed in the double mutant, implying that at least the median voltage activities are nonadditive. The Q_{max} values for single mutants and the double mutants were identical to those of the WT channels (Supplementary Fig. 2); therefore, the calculated $\Delta\Delta G$ of interaction is -5.37 ± 0.5 kcal/mol, indicating a relative stabilization of the activated state. This interaction energy is significantly above our cutoff of 1.8 kcal/mol of functional channels, which corresponds to 0.45 kcal/mol for each subunit. Given that this interaction is between an arginine and phenylalanine, it is quite likely that these two residues form an unusually strong cation–π interaction[35], stabilizing the activated state.

Next, we tested a triad of residues located at the intersection of S4 (S376) and the S4–S5 linker (L382 and Q383). We observed that the Q–V curves of single mutants L382A and S376A and the corresponding double mutant S376A L382A all shift left relative to that of the WT. Q_{max} measurements (Supplementary Fig. 2) show that these mutations apparently alter the total charge per channel, but we wondered whether a significant fraction of the total charge

moves at potentials beyond +50 mV. Previously, the L382V mutation has been shown to move a substantial fraction of the total charge at potentials corresponding to channel opening, which is also extremely right shifted compared to the WT[36,37]. Our measurements of G–V curves show that channel opening is also highly right shifted for both L382A and S376A L382A mutants (Supplementary Fig. 3 and Supplementary Dataset 3). To correctly account for all of the gating charge per channel, Q–V curves have to be extended to potentials at which the G–V curves saturate. However, we were not able to obtain reliable Q–V measurements beyond +50 mV using the cut-open-oocyte method because of the low expression of these mutants and increased endogenous currents at those potentials. Given these issues, we were unable to determine unambiguously whether these two sites interact, although both of these sites have been shown to be crucial for concerted final opening transitions[24,38–40]. On the other hand, similar analysis of S376 and Q383 showed that these mutations do not modify the Q_{max}. Taking the shifts in the Q–V curve into account, we determined that the interaction energy between these two positions is 0.57 ± 0.4 kcal/mol (Supplementary Table 2 and Supplementary Dataset 4). Thus, even though S376 is important for concerted transitions, its interaction with the Q383 site does not appear to change during channel gating.

Coupling interaction clusters at transmembrane gating interface. In channels with domain-swapped architecture, the S4 helix forms an interface with the S5 helix of the neighboring subunit. Mutations in this region have been shown to affect channel gating[23,25,41,42]. In particular, I372 and V369 are part of the well-studied ILT triple mutant[24]. Our measurements revealed that the interaction energy between I372 and I405 is −2.45 ± 0.4 kcal/mol and that between I372 and L409 is −4.15 ± 0.5 kcal/mol (Fig. 3 and Supplementary Table 2). Because the G–V curves of all I372A mutants are far-right shifted (Supplementary Fig. 3) and the Q_{max} values (Supplementary Fig. 2) calculated at +50 mV are lower than that of the WT, these pairs should be considered apparent interactors that stabilize the activated state, as discussed previously.

We next examined the interaction between V369 (S4) with V408 and S412 in the S5 segment. Our measurements show that the interaction energy between V369 and V408 is −2.2 ± 0.9 kcal/mol, whereas that between V369 and S412 is +1.79 ± 0.8 kcal/mol (Fig. 3 and Supplementary Table 2). Thus, both of these pairs interact, but, interestingly, the V369–V408 interaction is a stabilizing interaction in the activated state, whereas the V369–S412 interaction is destabilizing. Despite uncertainties of gating-interaction measurements at other sites, these findings unambiguously establish that specific residues in S4 and S5 transmembrane helices interact to drive electromechanical coupling in the Shaker K^+ channel.

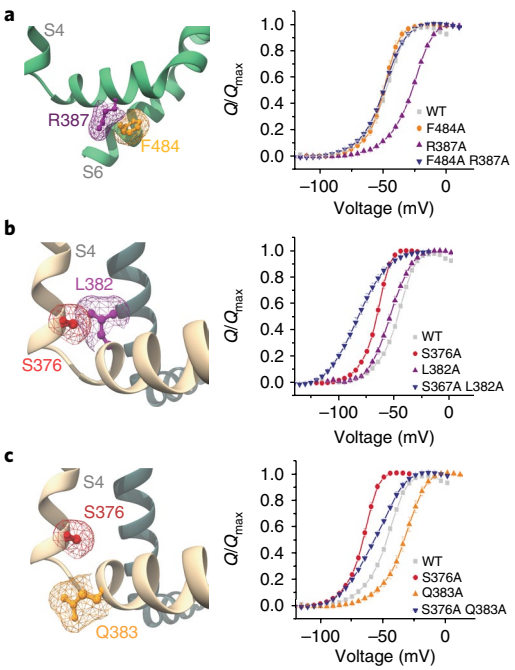

Fig. 2 | Interaction-energy analysis of residues in the intracellular gating interface. a, Left, side view of F484 (orange) and R387 (purple) mapped on the K_v1.2-2.1 chimera structure. Only the S4–S5 and S6 domains of the same subunit are shown for clarity. Right, normalized Q–V curves of WT, F484A, R387A and R387A F484A. **b**, Left, side view of S376 (red) and L382 (purple). S376 is at the end of the S4 segment, and L382 is at the beginning of the S4–S5 linker in the same subunit. Right, normalized Q–V curves of WT, S376A, L382A and S376A L382A. **c**, Left, side view of S376 (red) and Q383 (orange), which is at the start of the S4–S5 linker. Right, normalized Q–V curves of WT, S376, Q383A and S376A Q383A. Mesh in **a**–**c** represents the surface based on the Van der Waals radii for selected atoms. For Q–V plots, data shown are mean ± s.e.m. Source data are available in Supplementary Dataset 2.

Long-range interactions at the gating interfaces. In the last set of experiments, we explored interactions between pairs of residues that are not in direct steric contacts but are likely to be part of the energy transduction pathway between the voltage-sensor domain and the pore. Although a network of long-range interactors had been identified previously using functional mutant cycle analysis in the Shaker K^+ channel[43,44], a follow-up analysis using GIA showed that many of these were false positives[26]. Here, we measure gating interaction energies between V369 and S376 (bottom of S4) and R387, which is in the S4–S5 linker.

The interaction energy between V369 and S376 is 5.09 ± 0.75 kcal/mol, whereas that between V369 and R387 is 2.64 ± 0.71 kcal/mol. Thus, perturbations at V369 are transmitted to residues in the bottom part of the S4 helix and to those in the S4–S5 linker. These findings also show that the GIA method is not just limited to identifying residues that are involved in short-range interactions, but it can also be useful to track the long-range interaction pathways (Fig. 4 and Supplementary Table 2).

Network analysis of molecular dynamics trajectories. To reveal the structural details of the allosteric pathways linking the voltage-sensor domain and the pore, we analyzed multimicrosecond simulations of the resting (closed) and the activated (open) states of the K_v1.2–2.1 chimera produced by Jensen et al.[21] using network analysis. In brief, we constructed a network in which the nodes represent protein residues and the edges represent interactions between pairs of residues. The weight of the edges is a measure of how efficiently information is transferred from one residue to another, determined by measuring how the fluctuations of residue pairs covary over the course of the simulation. The underlying premise is that if the pairs interact tightly, the covariance will be high. Mathematically, the weights of the edges are information distances between residue pairs (measured as negative logarithm of the covariance measurements of pairs in contact more than 75% of the trajectory time) (Methods). This analysis can be carried out between all possible residue pairs to identify residues that are on pathways with short information distances (or conversely, of high covariance, from here on referred to as shortest pathways). Typically, network analyses are carried out on MD trajectories obtained from a single initial structure. However, here, we carried out independent network analyses on a trajectory of the crystallographic activated state structures and of a resting state model (obtained from long-time-scale simulations[21]). This approach allowed us to draw comparisons with our experimental data, which measure the changes in gating interactions as the

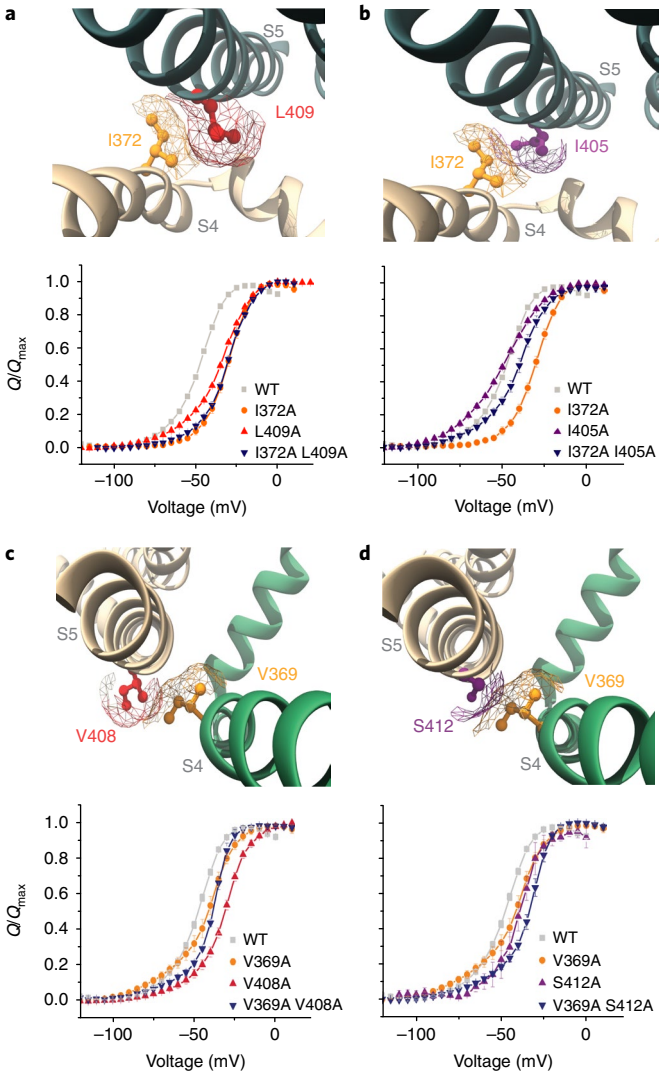

Fig. 3 | Interaction-energy analysis of residues in the transmembrane gating interface. a–d, Top, top-down view of the S4 and S5 helices from neighboring subunits obtained from the $K_v1.2$–2.1 chimera structure. Bottom, normalized Q-V curves for WT and indicated mutants. The structures in **a** and **b** feature residues I372 (orange), L409 (red) and I405 (purple), and structures in **c** and **d** feature residues V369 (orange), V408 (red) and S412 (purple). The mesh in the structures represents the surface based on the Van der Waals radii for the residue within the helix. Please note that only the mesh for the selected residue is shown. Source data for curves are in Supplementary Dataset 2.

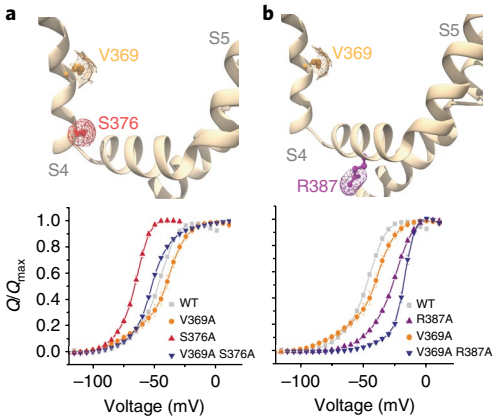

Fig. 4 | Long-distance interactions between the S4 and the S4–S5 linker of the same subunit. a,b Top panels show side views of S4 and the S4–S5 linker from the same subunit of the $K_v1.2$–2.1 chimera structure; mapped on the structure are residues V369 (orange), S376 (red) and R387 (purple). The mesh represents the surface based on the Van der Waals radii for the selected residue. Bottom panels show normalized Q-V curves for WT and indicated mutants. Source data for curves are in Supplementary Dataset 2.

channel goes from the resting to the activated state. We focused on the pathway linking R365, the residue on Shaker that moves the most gating charge, and V474 (using the Shaker K_V numbering for consistency), which is part of the narrow PVP motif on the S6 helix that constricts during pore closure[33,45–47].

The shortest pathways present in the activated state simulation can be classified into two modes of allosteric transmission (Supplementary Fig. 4a–d). One mode, present in two subunits, shows the pathway moving down S4, along the S4–S5 linker and then across to S6 (Supplementary Fig. 4a,b). The other mode shows the pathway first moving to the neighboring S5 subunit rather than moving down S4 (Supplementary Fig. 4c,d). To account for pathways originating in the rest of the voltage-sensor domain, we measured the shortest pathways linking residues located on average in a sphere of 9-Å radius from R365 and the V474 gate residue (details in Methods and Supplementary Table 3). In order to identify the key residues involved in allosteric coupling, we calculated the number of times a specific residue is present on the shortest pathway between voltage-sensor-domain residues in a 9-Å-radius sphere around R365 and the V474 gate residue (a quantity known as betweenness) (Fig. 5). Residues with high betweenness are hubs in the network because many shortest paths travel through these residues. This implies that these residues are important for the transfer of information between the voltage-sensor and pore domains. When multiple voltage-sensor-domain residues are considered as the origin of the allosteric pathway, the pathways are more degenerate, but the structural trend of having two subunits where the pathway is dominated by the intrasubunit mode while the other two subunits are dominated by the intersubunit mode remains (Fig. 5). In this way, these modalities are shown to be robust to a range of specific starting residues on the voltage sensor. Unlike the activated state, the resting state showed an intrasubunit pathway in each of the four subunits (Supplementary Fig. 4g–l). This difference in connectivity in the resting versus activated states suggests that the intersubunit pathway is a unique feature of the activated state. This notion is also consistent with our experimental data showing that the three interaction pairs between residues located on S4 and S5, 372–405, 372–409 and 369–408, are stabilized in the activated state.

Regarding the long-range interactions identified experimentally, V369–S376 and V369–R387, the network analysis shows that for one subunit in the activated state, both V369 and S376 fall on the optimal pathway and have a betweenness of 3 and 4.5, respectively (considerably higher than the average betweenness of all residues on these pathways, 1.63 ± 1.94) (Supplementary Fig. 4m). In the resting state, for one subunit, V369 and R387 fall on the optimal pathway and have betweenness values of 2.0 and 6.5, respectively (with an average betweenness of all residues of 2.77 ± 2.7) (Supplementary Fig. 4n). These long-range interactions may occur because the voltage-sensing process requires coupling of two domains over considerable distance and therefore can be perturbed by modulating residues that fall along this pathway. More pertinently, the fact that these long-range interactions are determined experimentally and can also be independently deduced from simulations indicates a remarkable congruity of such approaches.

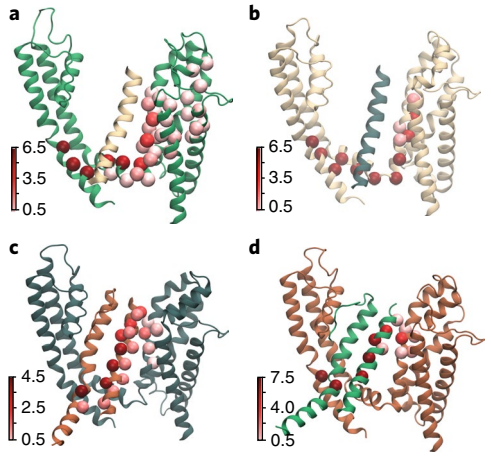

Fig. 5 | Residue betweenness for pathways between S4 and S6 in the activated (open) state. Betweenness is a measure of centrality of a residue in various allosteric pathways that link source and sink residues in that it calculates the number of shortest paths on which a residue falls. Residues with higher betweenness are hubs in the network and are therefore important for information flow along the network. Betweenness is calculated for residues of each individual subunit, because in MD simulations, each subunit evolves differently over time, owing to the stochasticity inherent in this process. **a**–**d**, Each panel represents one of the four subunits for which the subunit coloring and source and sink residues were selected following the convention described in Fig. 1. Residue betweenness for each subunit is mapped on to the activated state structures. Betweenness is calculated using source residues, where the Cα is, on average, within 9 Å of Arg365. Residues with high betweenness are shown in dark red, whereas low-betweenness residues are shown in light red. **a**,**b**, Residues of high betweenness are within a single subunit and travel down S4 and along the S4–S5 linker, finally linking up with the gate residues in the S6 subunit. **c**,**d**, Residues of high betweenness are on multiple subunits and travel from S4 to the neighboring subunit S5, then down the S5 helix. In these panels, the S6 helix of the neighboring subunit is also shown to identify the position of the sink residue. The intersubunit pathway remains consistent regardless of whether the sink residue is on the same or the adjacent subunit (Supplementary Fig. 4g,h).

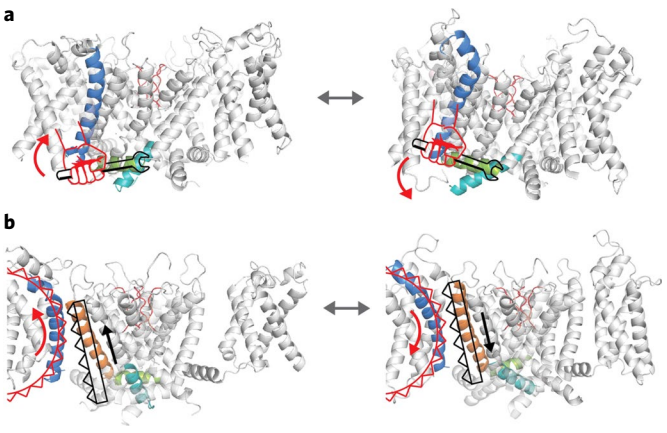

Fig. 6 | Schematic showing the two potential modes of electromechanical coupling in a prototypical potassium channel. a, In the canonical mode, S4 (blue) acts a lever arm moving the S4–S5 linker (green) directly, thereby causing the lower half of the S6 helix (cyan) to readjust. In the resting state, the S4 helix is down, which, through the S4–S5 linker, keeps the lower half of S6 in the closed state (left). When the S4 helix is up, the S4–S5 linker rotates upward and allows the lower S6 helices to splay open (right). **b**, Proposed alternate pathway. Gear-like movement of S4 helices directly shifts the position of the neighboring S5 helix. This movement is shown in Supplementary Video 1. In this rack-and-pinion type of coupling, when S4 is in the resting state (left), it holds the S5 helix in a down position, which forces the S6 gates to remain closed. The upward movement of the S4 helix (right) drives the S5 helix up and causes the S6 helices to open.

Discussion

Mutations of residues in the S4–S5 linker and the C-terminal end of the S6 region impair the activation of channel opening and voltage-sensor movement in a manner consistent with models that predict a loss of coupling[4,9,31]. According to the canonical model (Fig. 6a), upward movement of the S4 segment exerts a torque on the S4–S5 linker, which moves like a lever arm and allows the helices of $S6_{CT}$ to rotate outward, resulting in an open channel[19]. These mutations in the intracellular gating interface presumably disrupt the noncovalent interactions between the S4–S5 and $S6_{CT}$.The upshot of this model is that voltage sensing is considered to be a relatively independent module with very few meaningful tertiary contacts with the pore domain, especially within the membrane[48]. Indeed, it has been shown that the voltage-sensing module from *Ciona intestinalis* phosphatase can drive the voltage-dependent opening of the pore in viral potassium channels[49].

Nevertheless, mutations in residues on the S4 and S5 transmembrane segments are also known to exhibit a phenotype corresponding to a loss of coupling[24,25,42], thus raising the possibility that there are alternate pathways of electromechanical coupling. These pathways are presumably more important in non-domain-swapped channels in which the S4–S5 linker is either nonexistent or truncated[12,14,50]. Our study reveals that specific interaction pathways involving residues in the S4 and S5 transmembrane segments mediate voltage-dependent activation of the channel pore. Therefore, in addition to the intracellular gating interface, the transmembrane gating interface plays a central role in electromechanical coupling in the Shaker K^+ channel. While we do not have a quantitative estimate of the relative contributions of each of the two pathways, it is clear that the disruption of the transmembrane pathway dramatically reduces the coupling between the two modules.

Taking into account our findings from both experiments and network analysis, we can speculate upon the mechanism of how the two different pathways combine to control pore gating. Examination of the MD trajectory corresponding to an ultra-long simulation of a single $K_v1.2$–2.1 chimera suggests a possible alternate mechanism of voltage-sensor pore coupling. In response to hyperpolarizing voltage, the S4 undergoes a helical screw movement, but the pitch of the screw axis describing this movement is longer than an α-helix; the second arginine rotates about 90° anticlockwise and undergoes a translation corresponding to two helical turns (Supplementary Video 1). Thus, S4 residues that act like cogs of a pinion drive the interacting S5 helix (rack) downward (about half a helical turn) (Fig. 6b). Thus, the gear ratio between S4 and S5 movements is about 4:1. This displacement of S5 and the movement of the S4 push the S4–S5 linker, which directly regulates the position of the S6 gates. This rack-and-pinion type of coupling between voltage sensors and pore gates could be the primary mode of coupling in EAG or other non-domain-swapped channels. The difference being that rather than the S4–S5 linker, the position of S5 may directly influence the conformation of the S6 gates in those channels.

The number of trans interactions identified in this study was limited in part owing to the shortcomings of our approach. GIA provides estimates of interactions between specific residues if and only if the interaction strength changes upon channel activation. Thus, by definition, we can only identify interactions that contribute to the net free energy of open–closed equilibrium and not to the other class of coupling interactions that contribute to interactions only in the intermediate states[28,31]. For instance, interactions that

increase the strength of positive coupling by destabilizing the intermediate states will result in a steeper voltage-dependent opening. The other limitation of this method is that, experimentally, it is still difficult to accurately estimate the charge per channel. The errors associated with these measurements are relatively large. In some cases, we were not able to measure the full Q–V curve, because a considerable fraction of the charge moves at highly positive potentials (Supplementary Figs. 2–4).

Network analysis reduces the dimensionality of complex motions that occur during MD simulations. With a network of residues, it is possible to describe pathways of interactions that are difficult to quantify using other methods. Network theory has been successfully applied to understand other interaction interfaces, such as amino acid tRNA synthetase: tRNA interface and long-range interactions between substrate binding and the gate in the LeuT transporter[51,52]. While covariance is a proxy for interactions between residues, as opposed to a method such as free energy perturbation, which rigorously calculates this interaction energy, the fact that covariance can be calculated for all residues simultaneously provides for richer exploratory analysis. Therefore, in combination with network theory, covariance measurements provide a unique and more efficient approach to elucidate pathways that link distant moving parts of the channel.

Nevertheless, it is quite remarkable that despite the limitations of experimental and computational approaches, both delineate the same two pathways in voltage sensor–pore coupling. Unlike the canonical pathway, the pathway involving the transmembrane gating interface may be common to both domain-swapped and non-domain-swapped channels. Indeed, in the non-domain-swapped channels, this noncanonical pathway appears to be the only pathway involved in voltage transduction[11], but further studies are needed to test the generality of these ideas.

Methods

Methods, including statements of data availability and any associated accession codes and references, are available at https://doi.org/10.1038/s41594-018-0047-3.

Received: 29 September 2017; Accepted: 5 February 2018;
Published online: 26 March 2018

References

1. Long, S. B., Campbell, E. B. & Mackinnon, R. Crystal structure of a mammalian voltage-dependent Shaker family K+channel. *Science* **309**, 897–903 (2005).
2. Männikkö, R., Elinder, F. & Larsson, H. P. Voltage-sensing mechanism is conserved among ion channels gated by opposite voltages. *Nature* **419**, 837–841 (2002).
3. Larsson, H. P. The search is on for the voltage sensor-to-gate coupling. *J. Gen. Physiol.* **120**, 475–481 (2002).
4. Lu, Z., Klem, A. M. & Ramu, Y. Ion conduction pore is conserved among potassium channels. *Nature* **413**, 809–813 (2001).
5. Lu, Z., Klem, A. M. & Ramu, Y. Coupling between voltage sensors and activation gate in voltage-gated K+ channels. *J. Gen. Physiol.* **120**, 663–676 (2002).
6. Jiang, Y. et al. Crystal structure and mechanism of a calcium-gated potassium channel. *Nature* **417**, 515–522 (2002).
7. Guo, J. et al. Structure of the voltage-gated two-pore channel TPC1 from *Arabidopsis thaliana*. *Nature* **531**, 196–201 (2016).
8. Randich, A. M., Cuello, L. G., Wanderling, S. S. & Perozo, E. Biochemical and structural analysis of the hyperpolarization-activated K+ channel MVP. *Biochemistry.* **53**, 1627–1636 (2014).
9. Blunck, R. & Batulan, Z. Mechanism of electromechanical coupling in voltage-gated potassium channels. *Front. Pharmacol.* **3**, 166 (2012).
10. Hoshi, T., Pantazis, A. & Olcese, R. Transduction of voltage and Ca^{2+} signals by Slo1 BK channels. *Physiology (Bethesda).* **28**, 172–189 (2013).
11. Lörinczi, É. et al. Voltage-dependent gating of KCNH potassium channels lacking a covalent link between voltage-sensing and pore domains. *Nat. Commun.* **6**, 6672 (2015).
12. Lee, C. H. & MacKinnon, R. Structures of the human HCN1 hyperpolarization-activated channel. *Cell* **168**, 111–120.e11 (2017).
13. Payandeh, J., Gamal El-Din, T. M., Scheuer, T., Zheng, N. & Catterall, W. A. Crystal structure of a voltage-gated sodium channel in two potentially inactivated states. *Nature* **486**, 135–139 (2012).
14. Whicher, J. R. & MacKinnon, R. Structure of the voltage-gated K+ channel Eag1 reveals an alternative voltage sensing mechanism. *Science* **353**, 664–669 (2016).
15. Payandeh, J., Scheuer, T., Zheng, N. & Catterall, W. A. The crystal structure of a voltage-gated sodium channel. *Nature* **475**, 353–358 (2011).
16. Shen, H. et al. Structure of a eukaryotic voltage-gated sodium channel at near-atomic resolution. *Science* **355**, eaal4326 (2017).
17. Zhang, X. et al. Crystal structure of an orthologue of the NaChBac voltage-gated sodium channel. *Nature* **486**, 130–134 (2012).
18. Tsai, C. J. et al. Two alternative conformations of a voltage-gated sodium channel. *J. Mol. Biol.* **425**, 4074–4088 (2013).
19. Long, S. B., Campbell, E. B. & Mackinnon, R. Voltage sensor of Kv1.2: structural basis of electromechanical coupling. *Science* **309**, 903–908 (2005).
20. Wu, J. et al. Structure of the voltage-gated calcium channel Ca(v)1.1 at 3.6 Å resolution. *Nature* **537**, 191–196 (2016).
21. Jensen, M. O. et al. Mechanism of voltage gating in potassium channels. *Science* **336**, 229–233 (2012).
22. Vargas, E., Bezanilla, F. & Roux, B. In search of a consensus model of the resting state of a voltage-sensing domain. *Neuron.* **72**, 713–720 (2011).
23. Hackos, D. H., Chang, T. H. & Swartz, K. J. Scanning the intracellular S6 activation gate in the shaker K+channel. *J. Gen. Physiol.* **119**, 521–531 (2002).
24. Ledwell, J. L. A. & Aldrich, R. W. Mutations in the S4 region isolate the final voltage-dependent cooperative step in potassium channel activation. *J. Gen. Physiol.* **113**, 389–414 (1999).
25. Soler-Llavina, G. J., Chang, T. H. & Swartz, K. J. Functional interactions at the interface between voltage-sensing and pore domains in the Shaker K_v channel. *Neuron.* **52**, 623–634 (2006).
26. Chowdhury, S., Haehnel, B. M. & Chanda, B. A self-consistent approach for determining pairwise interactions that underlie channel activation. *J. Gen. Physiol.* **144**, 441–455 (2014).
27. Chowdhury, S., Haehnel, B. M. & Chanda, B. Interfacial gating triad is crucial for electromechanical transduction in voltage-activated potassium channels. *J. Gen. Physiol.* **144**, 457–467 (2014).
28. Chowdhury, S. & Chanda, B. Perspectives on: conformational coupling in ion channels: thermodynamics of electromechanical coupling in voltage-gated ion channels. *J. Gen. Physiol.* **140**, 613–623 (2012).
29. Miller, C. Model-free free energy for voltage-gated channels. *J. Gen. Physiol.* **139**, 1–2 (2012).
30. Yifrach, O. No model in mind: a model-free approach for studying ion channel gating. *J. Gen. Physiol.* **141**, 3–9 (2013).
31. Muroi, Y., Arcisio-Miranda, M., Chowdhury, S. & Chanda, B. Molecular determinants of coupling between the domain III voltage sensor and pore of a sodium channel. *Nat. Struct. Mol. Biol.* **17**, 230–237 (2010).
32. Batulan, Z., Haddad, G. A. & Blunck, R. An intersubunit interaction between S4-S5 linker and S6 is responsible for the slow off-gating component in Shaker K+ channels. *J. Biol. Chem.* **285**, 14005–14019 (2010).
33. Labro, A. J. et al. Kv channel gating requires a compatible S4-S5 linker and bottom part of S6, constrained by non-interacting residues. *J. Gen. Physiol.* **132**, 667–680 (2008).
34. Chen, J., Mitcheson, J. S., Tristani-Firouzi, M., Lin, M. & Sanguinetti, M. C. The S4-S5 linker couples voltage sensing and activation of pacemaker channels. *Proc. Natl Acad. Sci. USA* **98**, 11277–11282 (2001).
35. Pless, S. A. & Ahern, C. A. Introduction: applying chemical biology to ion channels. *Adv. Exp. Med. Biol.* **869**, 1–4 (2015).
36. Schoppa, N. E. & Sigworth, F. J. Activation of Shaker potassium channels. II. Kinetics of the V2 mutant channel. *J. Gen. Physiol.* **111**, 295–311 (1998).
37. Schoppa, N. E. & Sigworth, F. J. Activation of Shaker potassium channels. III. An activation gating model for wild-type and V2 mutant channels. *J. Gen. Physiol.* **111**, 313–342 (1998).
38. McCormack, K., Lin, L. & Sigworth, F. J. Substitution of a hydrophobic residue alters the conformational stability of Shaker K+channels during gating and assembly. *Biophys. J.* **65**, 1740–1748 (1993).
39. Smith-Maxwell, C. J., Ledwell, J. L. & Aldrich, R. W. Uncharged S4 residues and cooperativity in voltage-dependent potassium channel activation. *J. Gen. Physiol.* **111**, 421–439 (1998).
40. Smith-Maxwell, C. J., Ledwell, J. L. & Aldrich, R. W. Role of the S4 in cooperativity of voltage-dependent potassium channel activation. *J. Gen. Physiol.* **111**, 399–420 (1998).
41. Li-Smerin, Y., Hackos, D. H. & Swartz, K. J. A localized interaction surface for voltage-sensing domains on the pore domain of a K+channel. *Neuron.* **25**, 411–423 (2000).
42. Hong, K. H. & Miller, C. The lipid-protein interface of a Shaker K+ channel. *J. Gen. Physiol.* **115**, 51–58 (2000).

43. Sadovsky, E. & Yifrach, O. Principles underlying energetic coupling along an allosteric communication trajectory of a voltage-activated K+channel. *Proc. Natl Acad. Sci. USA* **104**, 19813–19818 (2007).
44. Yifrach, O. & MacKinnon, R. Energetics of pore opening in a voltage-gated K(+) channel. *Cell* **111**, 231–239 (2002).
45. del Camino, D., Holmgren, M., Liu, Y. & Yellen, G. Blocker protection in the pore of a voltage-gated K+channel and its structural implications. *Nature* **403**, 321–325 (2000).
46. Swartz, K. J. Structure and anticipatory movements of the S6 gate in Kv channels. *J. Gen. Physiol.* **126**, 413–417 (2005).
47. Jensen, M. O. et al. Principles of conduction and hydrophobic gating in K+channels. *Proc. Natl Acad. Sci. USA* **107**, 5833–5838 (2010).
48. Swartz, K. J. Sensing voltage across lipid membranes. *Nature* **456**, 891–897 (2008).
49. Arrigoni, C. et al. The voltage-sensing domain of a phosphatase gates the pore of a potassium channel. *J. Gen. Physiol.* **141**, 389–395 (2013).
50. Wang, W. & MacKinnon, R. Cryo-EM structure of the open human ether-a-go-go-related K+channel hERG. *Cell* **169**, 422–430.e10 (2017).
51. Sethi, A., Eargle, J., Black, A. A. & Luthey-Schulten, Z. Dynamical networks in tRNA:protein complexes. *Proc. Natl Acad. Sci. USA* **106**, 6620–6625 (2009).
52. LeVine, M. V. & Weinstein, H. NbIT–a new information theory-based analysis of allosteric mechanisms reveals residues that underlie function in the leucine transporter LeuT. *PLoS. Comput. Biol.* **10**, e1003603 (2014).

Acknowledgements

The authors thank K. Swartz and his colleagues for help with quantifying the expression of Shaker K^+ channel mutants during the early stages of this project. We also thank D. E. Shaw and colleagues for generously sharing the trajectories of long MD simulations and J. Cowgill for help making Fig. 6. The calculations were performed on resources provided by the Swedish National Infrastructure for Computing (SNIC) at PDC Centre for High Performance Computing (PDC-HPC). This research was supported by funding from NIH to B.C. (NS081293, GM084140 and NS101723) and K.O. (T32-HL07936). B.C. is also supported by Romnes Faculty Fellowship (WARF).

Author contributions

A.I.F.-M. contributed to design, acquisition and analysis of experimental data and writing the manuscript. T.J.H. carried out the network analyses, analyzed and interpreted the simulation data and contributed to writing the manuscript. K.O. contributed to design and acquisition of the experimental data. L.D. designed the network analyses, analyzed and interpreted data and contributed to writing the manuscript. B.C. conceived the project, designed experiments, interpreted data and wrote the manuscript.

Competing interests

The authors declare no competing interests.

Additional information

Supplementary information is available for this paper at https://doi.org/10.1038/s41594-018-0047-3.

Reprints and permissions information is available at www.nature.com/reprints.

Correspondence and requests for materials should be addressed to B.C.

Publisher's note: Springer Nature remains neutral with regard to jurisdictional claims in published maps and institutional affiliations.

Methods

Mutagenesis and expression in *Xenopus laevis* oocytes. All mutants were made in the fast inactivation-removed Shaker K_v channel (Δ6–46)[53] background using the QuickChange mutagenesis. For gating current measurements, the background is mCherry containing W434F construct. mCherry is inserted after the fifth residue in the N terminus. W434F renders the channel nonconducting[54] and facilitates gating current measurements. All mutations were confirmed by cDNA sequencing. Mutant cDNAs were linearized using NotI enzyme (Fermentas-Thermo Fisher Scientific) and transcribed into cRNAs using mMESSAGE mMACHINE T7 kit (Life Technologies).

Oocytes were purchased from Ecocyte or removed surgically from *Xenopus laevis* following protocols approved by the University of Wisconsin-Madison Institutional Animal Care and Use Committee. *Xenopus* oocytes were treated with 1 mg/ml collagenase for 1–1.5 h to remove the follicular layer. 50 nl cRNA at a concentration of 50–500 ng/μl was injected into oocytes. After the injection, oocytes were incubated in ND-96 solution supplemented with 100 U/ml penicillin-streptomycin, 50 μg/ml tetracycline, 0.1 mg/ml amikacin, 50 μg/ml ciprofloxacin, 100 μg/ml gentamicin and 0.5 mg/mL bovine serum albumin at 16 °C before the recording. Ionic current measurements were performed 24–48 h after injection, whereas gating currents were obtained 2–5 d after injection.

Electrophysiology. Gating currents were measured in a modified cut-open voltage clamp (COVG) setup (CA-1B; Dagan Corporation) as described previously[55]. The external solution used was 105 mM NMG, 10 mM HEPES, 2 mM CaOH, pH 7.4. The internal solution used was 105 mM NMG, 10 mM HEPES, 5 mM EGTA, pH 7.4. The recording pipette was filled with 3 M KCl. The microelectrode resistance for all electrophysiological measurements was 0.2–0.5 MΩ. Analog signals were sampled at 250 kHz with a Digidata 1440 A interface (Axon Instruments) and low-pass filtered at 10 KHz. Gating currents were obtained by applying a 200-ms depolarizing pulse to voltages from −150 mV to +100 mV every 5 mV. The holding potential used was −110 or −120 mV. Depolarization pulses were preceded by 50-ms pre- and post-pulses to −120 mV. The capacitive transients and linear leak currents were subtracted online using the P/−4 method with a substep holding potential of −110 mV. After baseline adjustments, the on-gating current records were integrated over the duration of the depolarization pulse to obtain the gating charge displaced, which was used to compute the fractional gating charge displacement versus voltage curve (Q/Q_{max} vs. V).

Ionic currents were also measured in a COVG set up (CA-1B; Dagan Corporation) as described previously[55]. The external solution used was 50 mM RbCl, 50 mM NaCl, 1 mM MgCl2 and 5 mM HEPES, pH 7.4. The internal solution was 95 mM RbCl, 5 mM NaCl, 2 mM EGTA and 5 mM HEPES, pH 7.4. Ionic currents were obtained by applying 50-ms depolarizing pulses from −120 mV to 190 mV every 3 mV. The holding potential was −110 mV. Capacitive transients and linear leak currents were subtracted online using the P/−4 method, during which the holding potential was −100 mV. After baseline subtraction, peak tail current amplitude, elicited by repolarization pulses to −110 mV, were used to generate the conductance versus voltage (G/G_{max} vs. V) curves.

Fluorescence measurements. Fluorescence and gating current measurements were obtained from the same oocyte on a customized cut-open fluorometry setup as described previously[55]. A xenon lamp (Hamamatsu Photonics) controlled by a feedback-stabilized power supply was used as an excitation light source. The microscope was equipped with a filter cube (excitation filter: 562/40, emission filter: 628/40 and dichroic 593 DiO_2) optimized for mCherry fluorescence measurements. Fluorescence measurements were obtained right before the gating current measurements. From a family of gating current traces, the maximum total charge (Q_{max}) was calculated and plotted with respect to the mCherry fluorescence intensity values.

Data analysis. The fractional gating charge displacement curves for all of the mutants were obtained by averaging measurements performed on at least five oocytes. The median voltage of activation, V_M, for each normalized Q–V curve was extracted by calculating the area between the Q–V curve and the ordinate axis using the trapezoid method. For a Q–V curve with n points, the V_M was calculated as:

$$V_M = \sum_{i=1}^{n-1} \frac{(Q_{(i+1)} - Q_{(i)})(V_{(i+1)} + V_{(i)})}{2}$$

Where Q_i and V_i correspond to charge and voltage for the i^{th} point on the Q–V curve. The net free energy of activation of the channel was calculated as $\Delta G_c = Q_{max} F V_M$, where Q_{max} is the maximum number of charges transferred during voltage-dependent activation of the channel.

In order to determine whether our point mutations alter the charge per channel, we calculated the relative Q_{max} value for each mutant using a modification of the fluorescence method described previously[56]. The absolute membrane fluorescence of each mCherry-tagged construct was measured along with the maximum voltage-dependent charge displacement going from a membrane potential of −120 mV to +50 mV. At these potentials, Q–V curves of most mutants were saturated, and the channels were fully open. Fluorescence intensity values were plotted against the Q_{max} from the same oocyte to obtain Fluo-Q_{max} scatter plots. We observed that the slopes of these scatter plots varied from batch to batch even for the WT channels, but within the same batch, they were tightly correlated. Therefore, for every mutant, we obtained Fluo-Q_{max} curves for the WT injected with the same batch. The slopes of the WT and mutant channels were calculated by linear regression. By using the equation (mutant slope / WT slope) × 13.2, we obtained Q_{max} values for the mutant (Supplementary Table 1). 13.2 is the total charge per channel for the Shaker K^+ channel, as estimated previously[57–59].

To determine the confidence intervals associated with fitting the Q_{max}-Fluo plots (Supplementary Fig. 5 and Supplementary Dataset 5), we performed a linear fitting using the Excel Software command LINEST. LINEST computes statistics for a least-squares straight line through a given set of data. From the data array, we computed the confidence intervals for every data point (with 95% confidence and n –2 degrees of freedom where n is the numbers of data points) by using the following equation:

$$dy_i = \pm t_{(0.05,dof)} SE_y(x) \sqrt{\frac{1}{n} + \frac{(\overline{x} - x_i)^2}{\sum_{i=1}^{n} (\overline{x} - x_i)^2}}$$

where t is the calculated t score corresponding to 95% confidence with n – 2 degrees of freedom; SEy is the standard error for the y estimate.

Given the errors of these Q_{max} measurements and that none of these mutations target the known gating charges in the Shaker K^+ channel, it is fair to assume that the mutations do not substantially alter the total charge per channel (Supplementary Fig. 2). In those few instances where the Q_{max} values for mutants were substantially lower than 13.2, we noted that the G–V curves (Supplementary Fig. 3 and Supplementary Table 1) are also far-right shifted, thereby indicating that the channels are not fully activated at + 50 mV. Some of these mutants are known to saturate at + 200 mV[24,36,37]. Because we are not able to reliably measure gating currents beyond + 50 mV with the cut-open-oocyte technique, we assumed that the total charge per channel is the same as that of the wild-type, although the median voltage values are quite different.

Interaction free energy between two positions was calculated by measuring the non-additivity in a mutant cycle based on the charge–voltage curves as described previously[26,27].Briefly, gating interaction free energy between sites S1 and S2 is:

$$\Delta\Delta G = Q_{max}\ F\,(V_{M(WT)} + V_{M(S12)} - V_{M(S1)} - V_{M(S2)})$$

where the subscripts WT stands for WT, S12 for double mutant and S1 and S2 for the two single mutants.

The uncertainty in interaction-energy calculation was calculated as $Q_{max}\ F\delta V_M$, where δV_M is the standard error of the V_M estimation. As described earlier, the Q_{max} values were considered to be unchanged. The standard error of gating interaction energy, $\delta\Delta\Delta G$, was calculated as:

$$\Delta\Delta G = Q_{max}\ F\sqrt{\{\delta(V_M)_{WT}\}^2 + \{\delta(V_M)_{S1}\}^2 + \{\delta(V_M)_{S2}\}^2 + \{\delta(V_M)_{S12}\}^2}$$

where $\delta(V_M)_{WT}$, $\delta(V_M)_{S1}$, $\delta(V_M)_{S2}$ and $\delta(V_M)_{S12}$ are the uncertainties (standard error of the mean) associated with V_M measurement of the WT channel and the single and the double mutant channels, respectively.

The G–V curves for each mutant were obtained by averaging the curves obtained from $n > 3$ oocytes. The curves were fitted individually to a Boltzmann equation:

$$\frac{G}{G_{max}} = \frac{1}{1 + \exp\left[\frac{zF(V_{1/2} - V)}{RT}\right]}$$

Where z is the Boltzmann slope and $V_{1/2}$ is the voltage that elicits half-maximal response.

Molecular simulations analyses. Molecular dynamics simulations of the K_v1.2–2.1 chimera structure in the activated and resting states from the D.E. Shaw group using Anton were analyzed[21]. The activated state corresponds to simulation 1 (77.85 μs in length) in Supplementary Table 1, and the resting state corresponds to simulation 9 (126 μs in length), where analysis began after ~10 e_0 of the gating charges were displaced (the last 72.2 μs of simulation 9). Residue-based networks were built and visualized using the Network View plugin within Visual Molecular Dynamics (VMD)[60,61]. The network is a residue-based matrix where each residue of the protein is a node (vertex), and edges (connections) between nodes are created for residues that are within a distance of 4.5 Å for at least 75% of the trajectory. Edge weights were calculated using −log (|C_{ij}|) where C_{ij} is the normalized covariance of Cα positions calculated using Carma[62]. C_{ij} and Δr_i are defined as:

$$C_{ij} = \frac{\langle \Delta\vec{r}_i(t) \cdot \Delta\vec{r}_j(t) \rangle_t}{\sqrt{\langle \Delta\vec{r}_i(t)^2 \rangle_t \langle \Delta\vec{r}_j(t)^2 \rangle_t}}$$

$$\Delta\vec{r}_i(t) = \vec{r}_i(t) - \langle \vec{r}_i(t) \rangle_t$$

Where $\langle\ \rangle_t$ denotes an ensemble average over time.

Shortest pathways and betweenness calculations were performed using the Dijkstra's algorithm as implemented in the NetworkX python library[63]. Betweenness calculations using a sphere of residues as source(starting) nodes were calculated using the average Cα distance during the simulation. We calculated betweenness for each subunit as the source radii was expanded and found that when the R365 residue was used as a source, betweeness values saturated at 9 Å in all the subunits (data not shown). Visualization and image creation of networks was done using VMD[61].

Because the $K_v1.2$–2.1 and shaker K_v channels are not completely homologous, a sequence alignment between the crystal structure of $K_v1.2$–2.1 and the shaker channels sequence was performed in order to determine residues that are at homologous sites between the two channels (Supplementary Fig. 6).

Life Sciences Reporting Summary. Further information on experimental design is available in the Life Sciences Reporting Summary.

Data availability. Source data for Figs. 2, 3 and 4 are available in Supplementary Dataset 2. Source data for Supplementary Figs 1, 3 and 5 are in Supplementary Datasets 3 and 5. The source values for free-energy calculations and Supplementary Table 1 is provided in Supplementary Datasets 1 and 4. Source data for Fig. 5 and Supplementary Fig. 4 is available from the corresponding author upon request.

References

53. Hoshi, T., Zagotta, W. N. & Aldrich, R. W. Shaker potassium channel gating. I: Transitions near the open state. *J. Gen. Physiol.* **103**, 249–278 (1994).
54. Perozo, E., MacKinnon, R., Bezanilla, F. & Stefani, E. Gating currents from a nonconducting mutant reveal open-closed conformations in Shaker K+channels. *Neuron.* **11**, 353–358 (1993).
55. Muroi, Y. & Chanda, B. Local anesthetics disrupt energetic coupling between the voltage-sensing segments of a sodium channel. *J. Gen. Physiol.* **133**, 1–15 (2009).
56. Gamal El-Din, T. M., Grögler, D., Lehmann, C., Heldstab, H. & Greeff, N. G. More gating charges are needed to open a Shaker K+channel than are needed to open an rBIIA Na+channel. *Biophys. J.* **95**, 1165–1175 (2008).
57. Seoh, S. A., Sigg, D., Papazian, D. M. & Bezanilla, F. Voltage-sensing residues in the S2 and S4 segments of the Shaker K+channel. *Neuron* **16**, 1159–1167 (1996).
58. Aggarwal, S. K. M. & MacKinnon, R. Contribution of the S4 segment to gating charge in the Shaker K+channel. *Neuron* **16**, 1169–1177 (1996).
59. Schoppa, N. E., McCormack, K., Tanouye, M. A. & Sigworth, F. J. The size of gating charge in wild-type and mutant Shaker potassium channels. *Science* **255**, 1712–1715 (1992).
60. Eargle, J. & Luthey-Schulten, Z. NetworkView: 3D display and analysis of protein·RNA interaction networks. *Bioinformatics* **28**, 3000–3001 (2012).
61. Humphrey, W., Dalke, A. & Schulten, K. VMD: visual molecular dynamics. *J. Mol. Graph.* **14**, 33–38 (1996).
62. Glykos, N. M. Software news and updates. Carma: a molecular dynamics analysis program. *J. Comput. Chem.* **27**, 1765–1768 (2006).
63. Hagberg, A. A., Schult, D. A. & Swart, P. J. Exploring network structure, dynamics, and function using NetworkX. In *Proc. 7th Python in Science Conference (SciPy 2008)* (Eds Varoquaux, G., Vaught, T. & Millman, J.) 11–15 (2008).

nature research

Corresponding author(s): Baron Chanda

☐ Initial submission ☐ Revised version ☒ Final submission

Life Sciences Reporting Summary

Nature Research wishes to improve the reproducibility of the work that we publish. This form is intended for publication with all accepted life science papers and provides structure for consistency and transparency in reporting. Every life science submission will use this form; some list items might not apply to an individual manuscript, but all fields must be completed for clarity.

For further information on the points included in this form, see Reporting Life Sciences Research. For further information on Nature Research policies, including our data availability policy, see Authors & Referees and the Editorial Policy Checklist.

Experimental design

1. Sample size

Describe how sample size was determined.

For electrophysiology recordings, a sample size of 5-10 oocytes were used for each mutant. This is typical in the field and the sample size for each mutant has been indicated in the data tables. Standard error means were reported and the propagated errors were also calculated.
For simulations, the networks were built using all possible configurations along the entire trajectories available from DE Shaw Research.

2. Data exclusions

Describe any data exclusions.

Oocytes showing signs of disease, (eg. infection) prior or during the acquisition data process were excluded.

3. Replication

Describe whether the experimental findings were reliably reproduced.

Yes! These measurements were reproduced.

4. Randomization

Describe how samples/organisms/participants were allocated into experimental groups.

Not Applicable.

5. Blinding

Describe whether the investigators were blinded to group allocation during data collection and/or analysis.

No

Note: all studies involving animals and/or human research participants must disclose whether blinding and randomization were used.

6. Statistical parameters

For all figures and tables that use statistical methods, confirm that the following items are present in relevant figure legends (or in the Methods section if additional space is needed).

n/a	Confirmed
☐	☒ The exact sample size (*n*) for each experimental group/condition, given as a discrete number and unit of measurement (animals, litters, cultures, etc.)
☐	☒ A description of how samples were collected, noting whether measurements were taken from distinct samples or whether the same sample was measured repeatedly
☐	☒ A statement indicating how many times each experiment was replicated
☒	☐ The statistical test(s) used and whether they are one- or two-sided (note: only common tests should be described solely by name; more complex techniques should be described in the Methods section)
☐	☒ A description of any assumptions or corrections, such as an adjustment for multiple comparisons
☐	☒ The test results (e.g. *P* values) given as exact values whenever possible and with confidence intervals noted
☐	☒ A clear description of statistics including central tendency (e.g. median, mean) and variation (e.g. standard deviation, interquartile range)
☐	☒ Clearly defined error bars

See the web collection on statistics for biologists for further resources and guidance.

Software

Policy information about availability of computer code

7. Software

Describe the software used to analyze the data in this study.	Residue-based networks were built and visualized using the Network View plugin within VMD. Shortest pathways and betweenness calculations were performed using the Dijkstra's algorithm as implemented in the NetworkX python library. Visualization and image creation of networks was done using VMD 1.9.2.

For manuscripts utilizing custom algorithms or software that are central to the paper but not yet described in the published literature, software must be made available to editors and reviewers upon request. We strongly encourage code deposition in a community repository (e.g. GitHub). *Nature Methods* guidance for providing algorithms and software for publication provides further information on this topic.

Materials and reagents

Policy information about availability of materials

8. Materials availability

Indicate whether there are restrictions on availability of unique materials or if these materials are only available for distribution by a for-profit company.	The trajectories for long time scale MD simulations are available on request from DE Shaw company. There is no restriction on other materials.

9. Antibodies

Describe the antibodies used and how they were validated for use in the system under study (i.e. assay and species).	None

10. Eukaryotic cell lines

a. State the source of each eukaryotic cell line used.	None used
b. Describe the method of cell line authentication used.	*Describe the authentication procedures for each cell line used OR declare that none of the cell lines used have been authenticated OR state that no eukaryotic cell lines were used.*
c. Report whether the cell lines were tested for mycoplasma contamination.	*Confirm that all cell lines tested negative for mycoplasma contamination OR describe the results of the testing for mycoplasma contamination OR declare that the cell lines were not tested for mycoplasma contamination OR state that no eukaryotic cell lines were used.*
d. If any of the cell lines used are listed in the database of commonly misidentified cell lines maintained by ICLAC, provide a scientific rationale for their use.	*Provide a rationale for the use of commonly misidentified cell lines OR state that no commonly misidentified cell lines were used.*

Animals and human research participants

Policy information about studies involving animals; when reporting animal research, follow the ARRIVE guidelines

11. Description of research animals

Provide details on animals and/or animal-derived materials used in the study.	Oocytes were either purchased from Ecocyte or harvested from Xenopus Laevis under University of Wisconsin-Madison IACUC approved animal protocols.

Policy information about studies involving human research participants

12. Description of human research participants

Describe the covariate-relevant population characteristics of the human research participants.	Not applicable